Sliding-mode position control of medium-stroke voice coil motor based on system identification observer

J. F. Pan[1, 2], *Member*, *IEEE*, Siu Wing Or[1*], *Senior Member*, *IEEE*, Yu Zou[1, 2], *Member*, *IEEE*, and Norbert C. Cheung[1], *Senior Member*, *IEEE*

[1]Department of Electrical Engineering, The Hong Kong Polytechnic University, Hung Hom, Kowloon, Hong Kong

[2]Shenzhen Key Laboratory of Electromagnetic Control, Shenzhen University, Shenzhen, China

Abstract – This paper presents the performance improvement in the position control of a medium-stroke voice coil motor (VCM) using a sliding-mode controller (SMC) with a system identification observer (SIO). The proposed VCM is developed with a full stroke of 24 mm, and its nonlinear electro-magneto-mechanical characteristics are analyzed by the three-dimensional finite element method. A least-squares-based SIO is introduced into the VCM control system prior to the position regulation of the SMC in order to achieve a shorter rise time of 29 ms and a smaller steady-state error of less than ± 2 μm under a square-wave excitation of 20 mm amplitude and 0.5 Hz frequency. An experimental verification between the SMC and a traditional proportion-integral-differential (PID) controller is carried out. The results demonstrate improved dynamic and static tracking responses in the SMC under load-free, frequency-varying operations.

Keywords – medium stroke, position control, sliding-mode controller, system identification observer, voice coil motor.

1   Introduction

The rapid development of high-precision manipulation, manufacturing, and testing equipment and facilities such as those for the semiconductor industry in recent years has put a high demand for direct-drive linear electric machines with full strokes ranging from 1 to 30 mm [1]. Voice coil motors (VCMs), because of their relatively small inertia, fast response, compact size, light weight, and low cost, have received much attention for short-stroke (0.1–1 mm) applications. Examples include high-density data systems [2], direct-drive valve systems [3], [4], auto-focusing mechanisms for digital cameras [5], etc. However, the short-stroke nature of VCMs often limits their widespread use even though they could be integrated with some other longer stroke machines such as linear synchronous permanent-magnet motors (LSPMMs) to increase the resulting strokes at the expense of deteriorating inertia, response, size, weight, and cost [6], [7]. Moreover, the nonlinear current–flux linkage–position characteristics of both VCMs and LSPMMs often cause difficulty in establishing precise mathematical models so that advanced control strategies are generally required to achieve desired position control performance [8].

To evaluate the high-frequency response and application of VCMs, a high-frequency direct-drive valve was developed based on a VCM having a full stroke of 1 mm and a nonlinear proportion-integral-differential (PID) controller [3]. A high-frequency VCM-based direct-drive servo valve was also realized using a state-space disturbance observer-based hybrid controller [4]. To overcome the problems of dynamically unknown models in VCM control

*Corresponding author: Siu Wing Or, email: eeswor@polyu.edu.hk

systems, an articulation control system based on an adaptive cerebellar model and a wavelet fuzzy compensator was proposed for VCMs, and maximum tracking errors of 1.562 and 1.418% were achieved under sinusoidal and periodic step commands, respectively [9]. To obtain a favorable chattering-free trajectory tracking performance in VCMs, a cerebellar model-based articulation controller combined with an adaptive dynamic sliding-mode fuzzy compensator was established to demonstrate an accurate trajectory tracking with reduced transient tracking error and chattering [10]. A sliding-mode friction compensator for tiny VCMs with a full stroke of 0.35 mm was demonstrated to have an absolute steady-state error of 4 μm in a compact camera module [11]. A VCM-driven optical image stabilizing system equipped with a fuzzy sliding-mode controller (SMC) was studied to correct the deviation in optical path caused by hand vibrations, and the results showed an improved performance compared to unit-feedback or PID controllers under step position command of 1 mm amplitude [12]. A VCM-actuated 3-axis servo gantry system with an internal model-based controller was found to have good tracking performance with a root-mean-square error of about 2 μm under periodic reference signals [13].

Up till now, there does not appear to be any solid works disclosing the design, modeling, and position control of VCMs having a medium full stroke of 1–30 mm. Nonetheless, the following researches on linear oscillatory machines (LOMs) could provide good references for developing medium-stroke VCMs [14]. A small permanent-magnet LOM and its test sequence were presented [15]. A thrust force optimization was performed on a flux-switching, yokeless translator-type LOM to exhibit an output force of 56% higher than a traditional linear LSPMM [16]. A nonlinear state-space model suitable for describing the transient states of LOMs was established and studied with good agreement with the experimental results [17]. A sensorless closed-loop position control strategy for LOMs was experimentally evaluated to demonstrate a reduced dynamic position error of less than 0.05 mm [18]. A super-twisting high-order sliding-mode direct torque control scheme for LOMs was inspected and found to have zero steady-state speed chattering with robust control behavior [19]. The scheme was extended to direct torque and flux control showing a speed chattering free operation and an excellent robustness [20].

On the side of sliding-mode control, a robust non-linear controller based on a second-order sliding-mode technique combined with block control linearization and super-twisting algorithm was reported in a doubly-fed induction generator [21]. An adaptive discrete-time tracking controller based on block-control and sliding-mode techniques was investigated [22]. An adaptive second-order sliding-mode control strategy for maximizing the energy production of a wind energy conversion system was reported [23]. The general criterion for designing multi-input multi-output homogeneous sliding modes for uncertain dynamic systems was examined, and the ultimate asymptotic accuracy was found to be preservative in both multi-input multi-output and single-input single-output systems [24].

Comparing to the reported works on VCMs, LOMs, and sliding-mode control, we have achieved three aspects of innovation in our current work. First, a medium-stroke VCM with a full stroke of 24 mm is constructed and modeled. Second, finite element method (FEM) is used to analyze the nonlinear electro-magneto-mechanical characteristics of the VCM and to study the effect of stroke on nonlinearity, especially for that near the edges of permanent magnets

(PMs). Third, a SMC with a least squares-based system identification observer (SIO) is proposed to overcome the nonlinear electro-magneto-mechanical characteristics of the VCM and to improve both the dynamic and static position control responses. The ultimate goal of the position control is to minimize the rise time and the steady-state error. Hence, a SIO based on least squares is introduced into the VCM control system before position-regulating the SMC.

The organization of this paper is as follows. The construction and modeling of the medium-stroke VCM are described in section 2. The investigation based on FEM is presented in section 3. The parameter identification and SMC design are given in section 4. The implementation results and conclusions are delivered in sections 5 and 6, respectively.

2 Construction and modeling of medium-stroke VCM

2.1 Construction

Figure 1 shows the structure of the proposed medium-stroke VCM. The VCM mainly consists of a stator with PMs and a mover. The base and inner core of the stator are made of aluminum alloy and inner core, respectively. The mover (winding and holder) is restricted to the axial motion between the air gap of the three arched PMs bonded in the base and the inner core. The winding holder is made of plastic. The major specification data are listed in Table I.
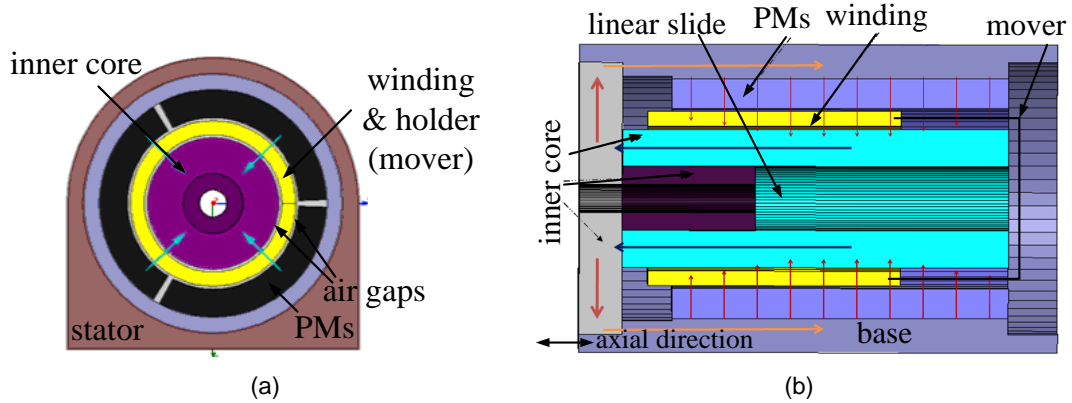

(a) (b)

Fig. 1 (a) front and (b) cross-section views of the medium-stroke VCM

Table 1 Major specification data

Parameter	Value
Mass of stator	1.0 kg
Mass of mover	0.2 kg
Air gap length	0.2 mm
Number of turns	1000
Permanent magnet type	NdFeB
Stator diameter	66.8 mm
Stator length	83.94 mm

2.2 Modeling

From the electrical side, the voltage balancing equation can be expressed as

$$u_{in} = R \cdot i + L \cdot \frac{di}{dt} + e_{\sigma}, \tag{1}$$

where u_{in}, R, i, L, and e_{σ} are the terminal voltage, winding resistance, current, inductance, and inductive electromotive force, respectively. In normal operations, e_{σ} can be written as [26]

$$e_{\sigma} = B(x) \cdot l \cdot v, \tag{2}$$

where $B(x)$, l, and v are the mover displacement dependent magnet flux density in the air gap, the length of the winding, and the speed of the mover, respectively. As B is a function of x and is not uniform in the whole stroke range, e_{σ} can further be expressed as

$$F(x,t) = K_1 \cdot B(x) \cdot l \cdot i(t), \tag{3}$$

where K_1 is the electromagnetic force coefficient.

From the mechanical side, the equation that governs the dynamic behavior of machines can be presented as

$$m\ddot{x} + K_v \dot{x} + F_L = F(x,t) = K_f(x) \cdot i(t), \tag{4}$$

$$K_f(x) = K_1 \cdot B(x) \cdot l \cdot i(t), \tag{5}$$

where m is the mass of the mover, K_v is the damping coefficient, and F_L is the load force.

The second-order continuous model with the consideration of stochastic noise $\varepsilon(t)$ can be written in discrete-time form as [27]

$$A(z^{-1}) \cdot x(t) = B(z^{-1}) \cdot F(t) + \varepsilon(t), \tag{6}$$

with $\begin{cases} A(z^{-1}) = 1 + a_1 \cdot z^{-1} + a_2 \cdot z^{-2} \\ B(z^{-1}) = b_0 + b_1 \cdot z^{-1} \end{cases}$,

where a_1, a_2 and b_0, b_1 depict the behavior of the VCM.

3 Investigation based on FEM

In order to investigate the nonlinear electro-magneto-mechanical characteristics of the VCM, a three-dimensional (3D) FEM model is constructed. Using the 3D time-stepping calculation method, the magnetic flux distribution contour at the fully overlapped position from the mover to the stator under a current excitation of 1 A is showed in Fig. 2(a). It is clear that magnetic flux lines distribute unevenly over the entire magnetic path and tend to saturation at the edges of the PMs because of the domination of magnetic flux circulation by end effect.

The propulsion force versus displacement at different current levels are plotted in Fig. 2(b),

where 0 mm stands for the fully overlapped position from the mover to the stator. Nonlinear characteristics are observed in the VCM. As the mover enters or leaves the stator base, the end effect becomes more significant at elevated current levels. The occurrence of maximum force at 14 mm for all currents suggests the existence of a linear relationship between the maximum force and the current. Thus, the electromagnetic force coefficient K_1 in Eq. (5) can be regarded as a function of displacement x.
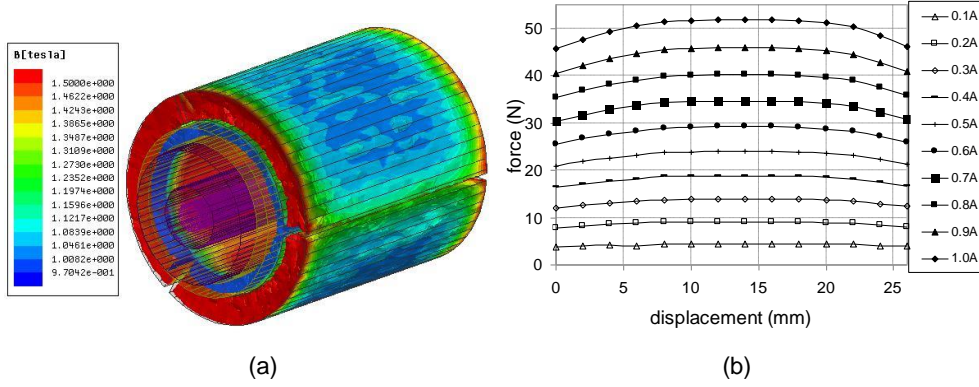

(a)   (b)

Fig. 2 FEM result of (a) magnetic flux distribution and (b) force vs current at different displacements

4   Parameter identification and SMC design

4.1 Online parameters identification with forgetting factor

For position control applications, Eq. (4) gives a physical meaning that the system input and output can be treated as force command F and displacement x, respectively. As denoted in Eq. (6), a_1, a_2 and b_0, b_1 are parameters to be estimated. Disturbances may influent the control system in any form. For the *N*-th estimation, the disturbances can be considered as stochastic errors, and the control system can be expressed by least squares form as [27]

$$X_N = \phi_N \theta + e_N,\tag{7}$$

where $\theta = [a_1, a_2, b_0, b_1]$, $\phi_N = [-X_{N-1,} - X_{N-2,}]$, and e is the residuals. ϕ_N includes the position information of the *N*-1-th and *N*-2-th experiments.

For the *N*+1-th experiment, θ can be estimated by the recursive least squares algorithm as [28]

$$\bar{\theta}_{N+1=} = \bar{\theta}_N + G_N[X_{N+1} - (\phi_{N+1})^T \bar{\theta}_N],\tag{8}$$

$$G_{N+1} = \frac{P_N \phi_{N+1}}{\rho + (\phi_{N+1})^T P_N \phi_{N+1}},\tag{9}$$

$$P_{N+1} = \frac{1}{\rho}[I - G_{N+1}(\phi_{N+1})^T]P_N,\tag{10}$$

where P is the covariance matrix, G is the gain matrix, and ρ is the forgetting factor with 0.99. For initial values, $P = \sigma I$ as $\sigma = 30$ and I is a 4×4 unit matrix. The initial values of

the parameters to be estimated from a_1 to b_1 are set to be zero.

The estimation termination criterion for the recursive calculation can be set as follows:

$$\left| \frac{\theta_{n+1} - \theta_n}{\theta_n} \right| < e_r . \tag{11}$$

If the maximum proportion of error from the last to the present estimated value is small compared to a positive number e_r, the estimation process will stop.

4.2 Force-to-current conversion

As depicted in Fig. 2(b), the force-displacement relationship at different current levels exhibits nonlinearity. To precisely derive current command for the current amplifier in the VCM control system, the measured output force in response to the current command is obtained as shown in Fig. 3. The data are stored in the one-dimensional look-up table for the linearization of current command to output force [29]. The position control block diagram is illustrated in Fig. 4.
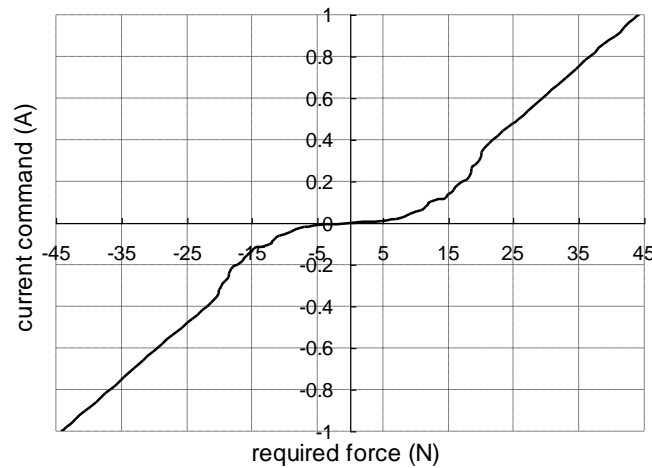

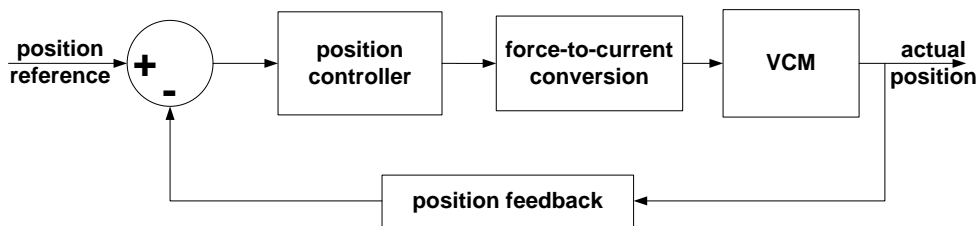Fig. 3 relationship of current command to output force

Fig. 4 position control block diagram

4.3 SMC design

For position controller, the relatively simple and effective PID controller can be employed and presented as

$$C(s) = K_p + K_i \cdot \frac{1}{s} + K_d \cdot s , \tag{12}$$

where K_p, K_i, and K_d are the proportional, integral, and differential gains, respectively.

According to the above analysis, the control plant can also be derived as a state-space model as

$$\begin{cases} \dot{x} = \begin{bmatrix} a_{11} & a_{12} \\ a_{21} & a_{22} \end{bmatrix} \cdot x + \begin{bmatrix} bb_1 \\ bb_2 \end{bmatrix} \cdot u \\ y = \begin{bmatrix} c_1 & c_2 \end{bmatrix} \cdot x \end{cases}, \tag{13}$$

where $a_{11}, a_{12}, a_{21}, a_{22}, bb_1, bb_2, c_1, c_2$ are the parameters of the VCM control system in state-space form, while $x = \begin{bmatrix} x(1) \\ x(2) \end{bmatrix}$, u, and y are the state variables, system input, and system output, respectively. Then, we have,

$$\dot{x}(2) = a_{21} \cdot x(1) + a_{22} \cdot x(2) + bb_2 \cdot u. \tag{14}$$

Assuming the reference command as r, the error and its derivative can be written as [31]

$$E = \begin{bmatrix} e \\ \dot{e} \end{bmatrix} = \begin{bmatrix} r - x(1) \\ \dot{r} - x(2) \end{bmatrix}. \tag{15}$$

If we set the gains of errors as $C = \begin{bmatrix} c & 1 \end{bmatrix}$, the switch function becomes

$$\begin{cases} s = CE \\ \dot{s} = c(\dot{r} - \dot{x}(1)) + \ddot{r} - \dot{x}(2) = slaw \end{cases}, \tag{16}$$

where $slaw$ is the trending law. To reduce the trending time and to make the speed approach to the switch sliding surface, the exponential trending law is selected as [32]

$$\dot{s} = -\varepsilon\,\text{sgn}(s) - ks \quad (\varepsilon > 0, k > 0), \tag{17}$$

where ε denotes the approaching speed to the switch sliding surface and k is the gain that demonstrates local reaching condition to the switch sliding surface. Substituting Eq. (14) into Eq. (16), the control output can be expressed as

$$u = \frac{1}{b_2}(c(\dot{r} - x(2)) + \ddot{r} - a_{21}x(1) - a_{22}x(2) - slaw). \tag{18}$$

Stabilization proof: For the closed loop system depicted in Eq. (17), considering the Lyaponov function and the global stability condition in the following forms

$$\begin{cases} V = \dfrac{1}{2}s^2(t) \\ \dot{V} = \dot{s}(t) \cdot s(t) < 0 \end{cases} \tag{19}$$

along with the trajectory of the solution for the closed-loop system, we obtain

$$\dot{s}s = -\varepsilon \cdot s \cdot \text{sgn}(s) - k \cdot s^2 \tag{20}$$

$s\,\mathrm{sgn}(s) > 0$, $\varepsilon > 0$ and $k > 0$ guarantees that $\dot{s}\,s < 0$. This completes the proof.

Figure 5 shows the position control flow chart. As the SIO requires a closed-loop operation of the control system, and since the sliding-mode control strategy depends on the SIO information after all the identification parameters are settled, PID position regulation is first implemented. After the configuration of P, I, and D gains from the PID position regulator, the processes of parameter initialization and sampling of force command and position output start. The control effort output is the force command of the VCM [30]. The force-to-current conversion module calculates the required current command for the current amplifier and then outputs the actual current to the VCM in a closed-loop current regulation manner.
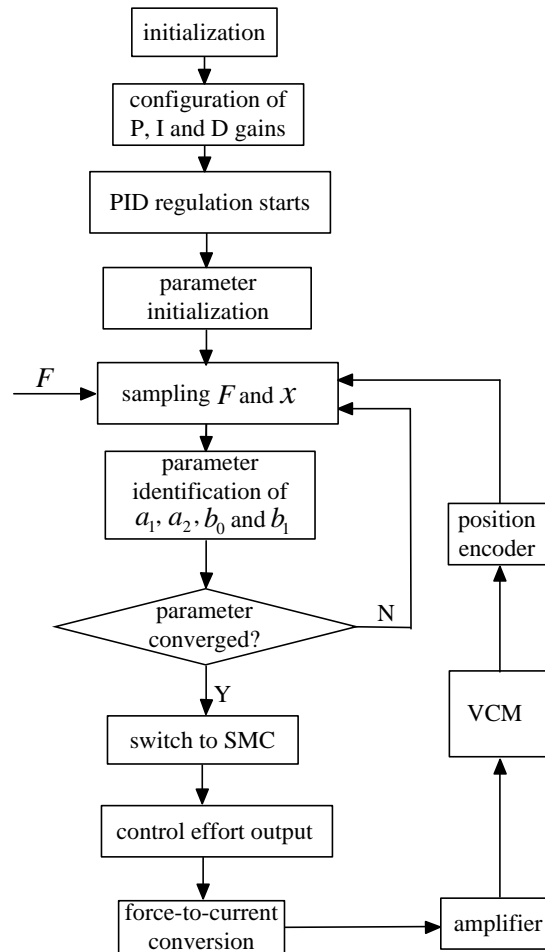
Fig. 5 position control flow chart

5 Implementation results

5.1 Simulation results

5.1.1 Parameter regulation

The position command is set as a square-wave signal with an amplitude of 20 mm and a frequency of 0.5 Hz for a load-free operation. The regulation of P, I, and D gains from the PID position controller are based on the tradeoff between fast rise time and small steady-state error from positive or negative transitions to enjoy an overshoot-free position response. The control parameters can be regulated based on trial and error with PID gains listed in Table II. After the parameter identification process is completed, the PID control method is switched to

the SMC. The control parameters of the SMC include *C*, *k*, and *ε*. Generally, bigger *C* and *k* values result in a faster response of the system performance [31]. *ε* is responsible for perturbation suppression. It is often selected as a tradeoff between the ability of disturbance rejection and system chattering, which is perceived as the oscillating motion about the sliding manifold [31]. For the VCM, the SMC parameters are regulated based on a chattering-free performance and the parameters are tabulated as shown in Table II.

Table II control gains

SMC parameter	Value
P	1.03
I	0.01
D	0.012
C	250
k	150.7
ε	2

Figures 6(a) and 6(b) demonstrate the position tracking and speed profiles of the SMC and PID. It is observed that all position tracking profiles enjoy an overshoot-free, zero steady-state performance. The rise time of the SMC is smaller than the PID regulator. It can also be deducted from the speed response waveforms that the dwell time is smaller for the SMC in either positive or negative transition.

(a)
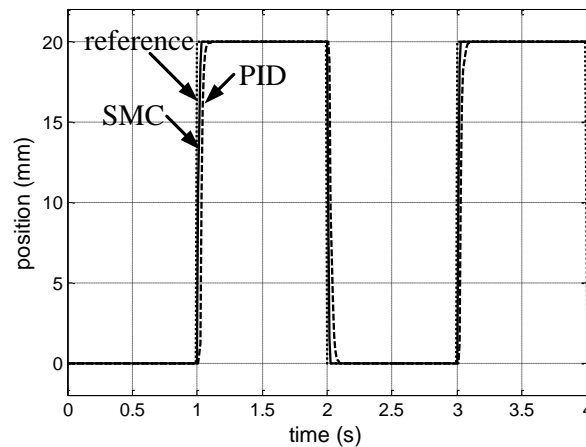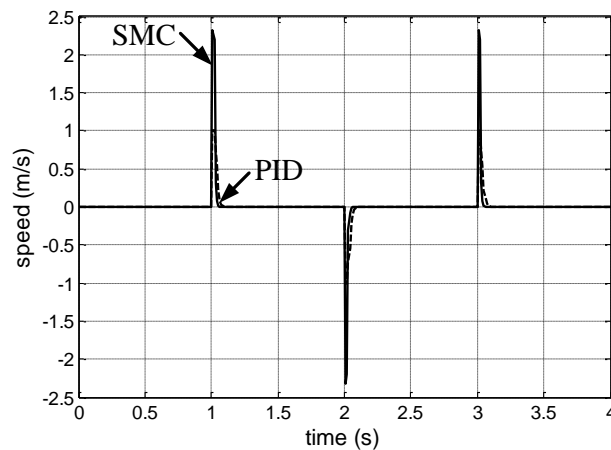
Fig. 6 simulation results of (a) position and (b) speed responses

5.2 Experimental results

5.2.1 Experimental setup

Figure 7(a) shows the experimental setup for evaluating the VCM and the SMC with SIO. The position control of the VCM was conducted in real time based on a dSPACE DS1104 controller card [33]. The sampling frequency of the position control loop was set at 1 kHz. The current amplifier was a commercial driver capable of providing an inner current regulation based on a proportion-integral algorithm with a sampling rate of 10 kHz. A linear magnetic encoder was mounted on the linear slide with a resolution of 1 μm. The control program was developed under MATLAB/SIMULINK which was directly downloaded to the DSP of the control board. The control parameters, reference profile, and response profiles were modified and supervised online.

5.2.2 Parameter identification

Figure 7(b) shows the converging profiles for the system parameters. In the initial parameter identification process, it takes about 7–9 seconds for all parameters to get settled from zero. After the control system enters the stable operation state, any tiny change in the parameters can be quickly identified and observed. Therefore, the speed of the SIO is fast enough for the position control regulation [29].
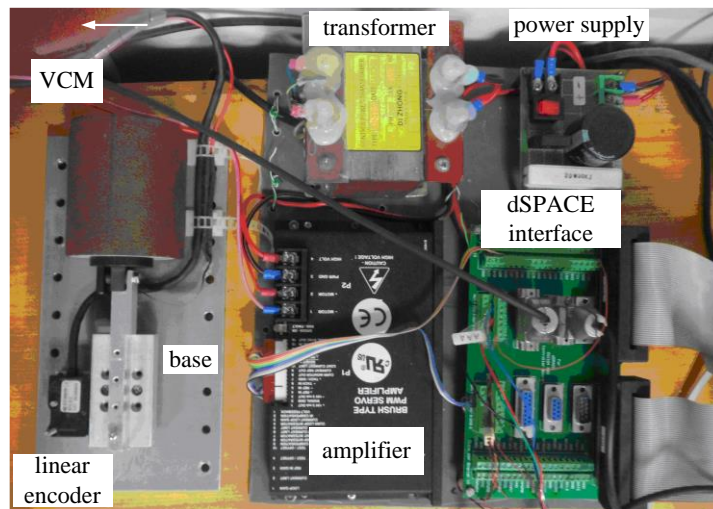

(a)
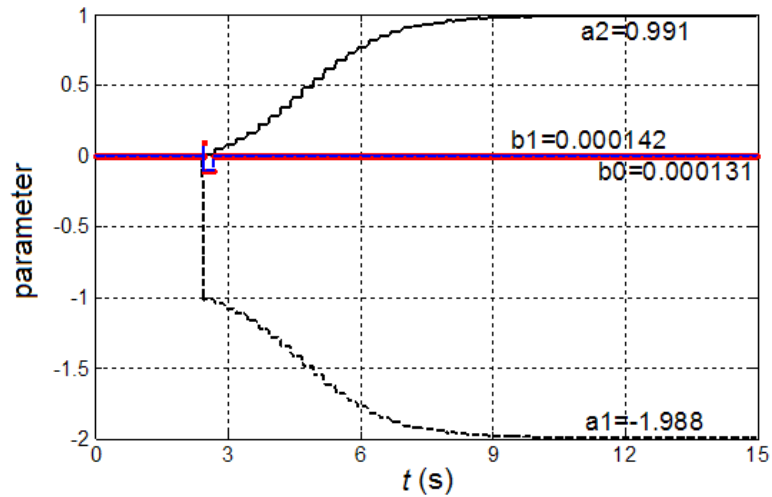
(b)

Fig. 7 (a) experiment setup and (b) parameter converging profiles

5.2.3 Control performance of PID controller

Figure 8(a) shows the dynamic position response of the PID control. The PID and SMC gains remain the same as listed in Table II. It is seen that the dynamic transitions of the positive and negative cycles are different since the mechanical characteristics such as uneven friction or air gap lengths, etc., from each direction of motion are not uniform. From the dynamic error response in Fig. 8(b), the tracking precisions of the rise and fall parts for the first half cycle are 12 and -76.5 μm, respectively. They change to 0.0481 and -0.0532 mm for the second half cycle. From the control effort output waveform in Fig. 8(c), the control effort output jumps sharply at 1 s, decreases gradually, but cannot conform to the reference signal at the stable state. The waveforms from different transitions are not symmetric as well. This can also be verified from the control effort output waveform in Fig. 8(c) in that there is a dominant regulation if sharp change in the reference signal occurs. It takes about 0.1 s for the response waveform to dwell and approach to the steady-state value.
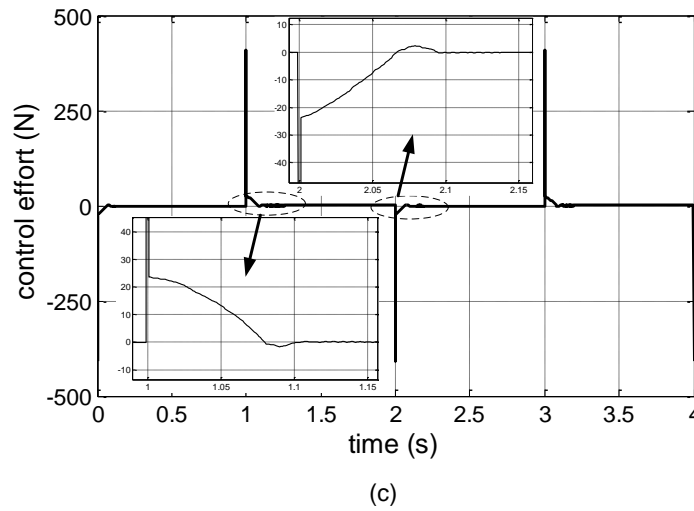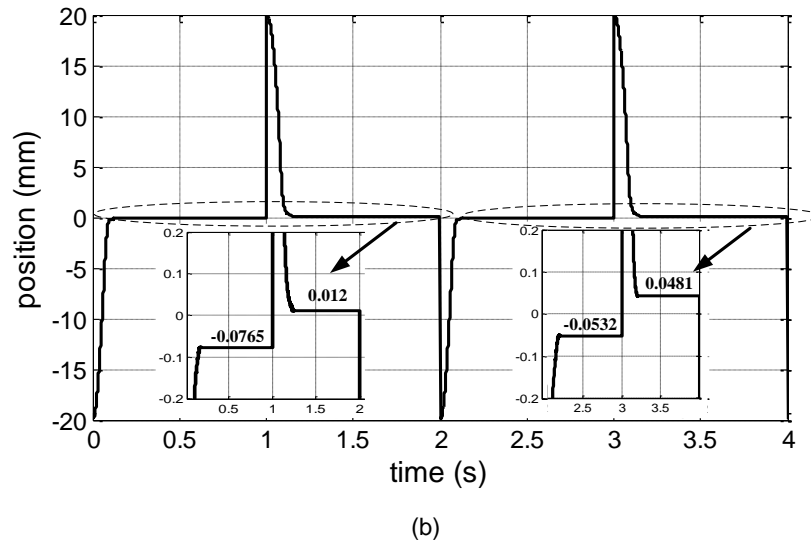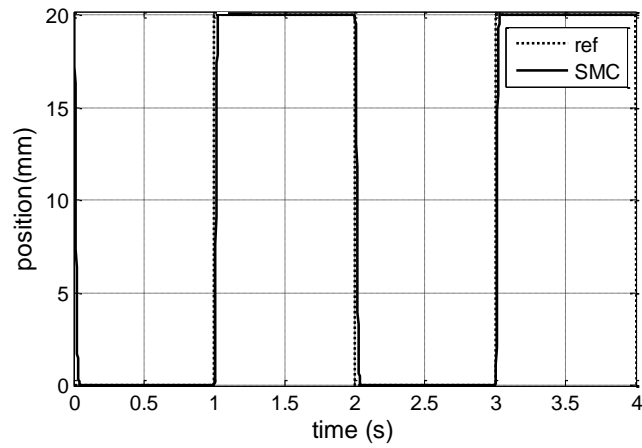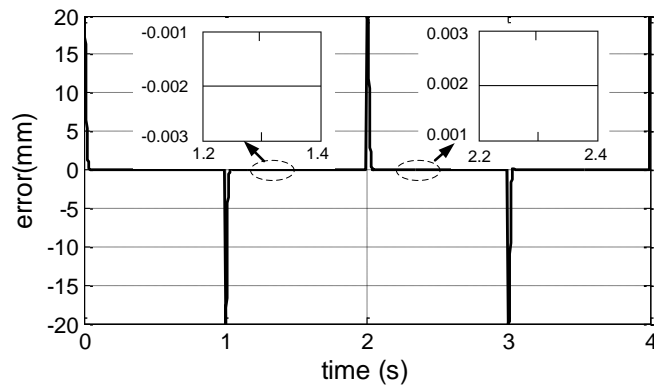

(a)

(b)

(c)
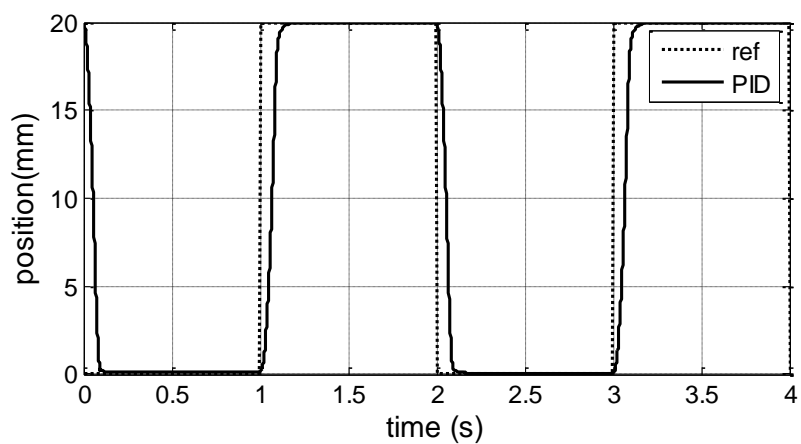
Fig. 8 position control performance of PID (a) dynamic response, (b) dynamic error response, and (c) control effort output

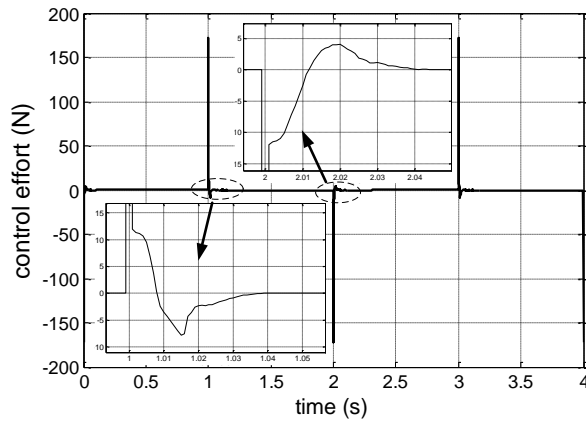*5.2.4 Control performance of SMC*

With the same operation position reference, Fig. 9 shows the position control performance of the SMC. From the dynamic position response in Fig. 9(a), a fast rise time and the symmetric behavior of the response are noticeable. From the dynamic error response in Fig. 9(b), the motion control system enters the steady state after a shorter duration compared to the PID controller. The absolute steady-state error is uniformly 2 μm, either for the positive or negative transition. From the control effort output waveform in Fig. 9(c), it can be verified that the regulation time is about 40 times shorter than the PID controller.

Fig. 9 position control performance of SMC (a) dynamic response, (b) dynamic error response, and (c) control effort output

Due to mechanical imperfections and unbalanced behaviors of the VCM, the control performance of the positive and negative transitions is not uniform for the PID controller. However, the SMC regulator is capable of providing a uniform tracking performance based on the online parameter identification observer. Table III tabulates the key control performance indices of the two position regulators. It can be concluded that the control performance is improved in the SMC regulator. The rise time is 13% shorter than the PID controller. In addition,

the tuning time of 2% bandwidth is about 20% compared to the PID controller. The control performance of the SMC with the observer ensures a uniform steady-state performance under load-free operation.

Table III Performance comparison between PID and SMC

controller	rise time	tuning time (2%)	steady-state error (+ transition)	steady-state error (- transition)	steady-state error to full stroke (%)
PID	0.229 s	0.121 s	12 μm	76 μm	≥0.6 ‰
SMC	0.029 s	0.025 s	2 μm	2 μm	0.1 ‰

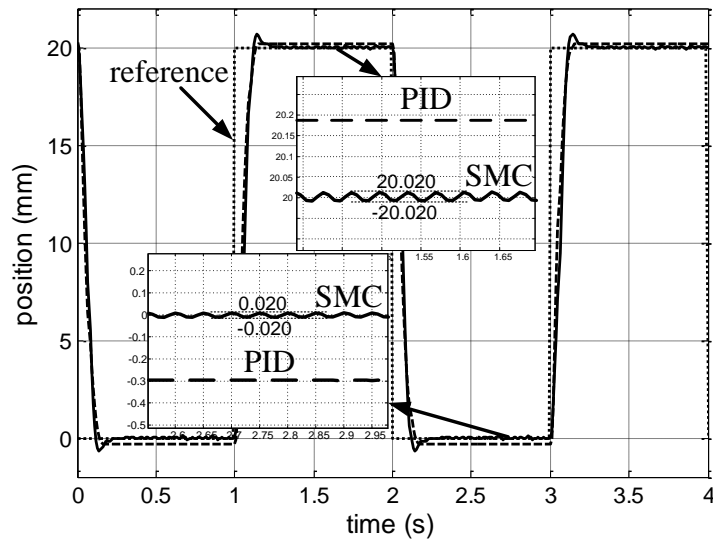*5.2.5 Control performance at 1 Hz reference*

As illustrated in Table II, with the control gains for the SMC and PID controller unchanged, the position reference signal is set as square wave of 20 mm amplitude and 1 Hz frequency. From the dynamic tracking profiles in Fig. 10(a), although the rise time of the positive transition is faster for the PID controller, the control behavior is not uniform for both the positive and negative transitions. The SMC is still able to give a uniform control performance with the absolute steady-state error within 2 μm.

5.2.6 Control performance at 50% load

At 0.5 Hz frequency and 500 g mass load, the load translates together with the moving platform, and the position tracking profiles can be found in Fig. 10(b). For the SMC, there exists considerable chattering in steady-state in the limit of $\pm$20 μm. For the PID controller, the behavior of each transition is still not uniform and the steady-state errors are 0.18 and -0.3 mm, respectively.
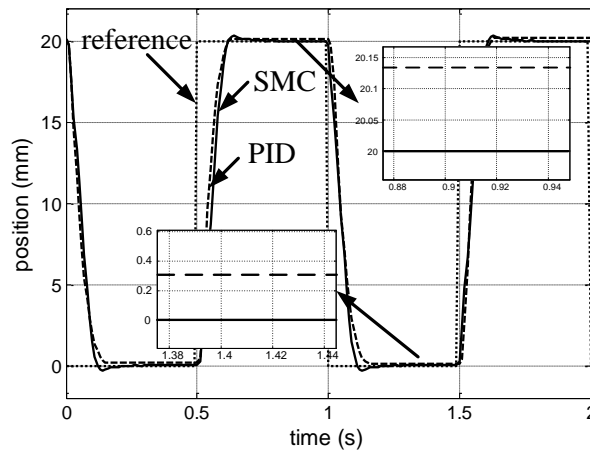
(a)

(b)

Fig. 10 (a) position control performance at 1 Hz reference and (b) at 50% load

6 Conclusion and Discussion

A medium-stroke VCM with a full stroke of 24 mm has been physically constructed, theoretically modeled, and computationally analyzed. A SMC with a least squares-based SIO has been proposed to overcome the nonlinear current–flux linkage–position characteristics of the VCM and to improve the position control performance by minimizing the rise time and the steady-state error. The control effectiveness of the SMC on the VCM has been experimentally verified and compared with a traditional PID controller. It has been found that the SMC possesses improved dynamic and static tracking responses under load-free, frequency-varying operations. Specifically, it demonstrates a shorter rise time of 29 ms and a smaller steady-state error of less than ± 2 μm at a square-wave excitation of 20 mm amplitude and 0.5 Hz frequency. Comparing to short-stroke VCM-actuated motion systems, a small value of 0.001 has been achieved in the ratio of steady-state error to full stroke at the condition of load free with the frequency variation to 1 Hz.

It has been reported that the super-twisting sliding-mode (STSM) control strategy possesses the features of a conventional sliding-mode control combined with the proportional integral algorithm to enjoy a steady-state chattering-free and robust behavior [19]. It is suitable for rotary PM or induction motors with direct torque regulations [19], [20]. Since the STSM has the ability to correct machine coupling and nonlinearity, the authors suggest evaluating the performance of the STSM on eliminating chattering and achieving a more robust behavior of the medium-stroke VCM under external load disturbances. A simple and straightforward STSM algorithm can be expected for easy implementation of digital VCM control systems based on single digital processing chips.

5   References

[1]   Panat, R., Wang, J., Parks, E., Effects of Triboelectrostatic Charging Between Polymer Surfaces in Manufacturing and Test of Integrated Circuit Packages, IEEE Transactions on Components, Packaging and Manufacturing Technology, vol. 4, no. 5, 2014, 943- 946

[2]   Djamari, D.W., Ong, C.J., Yap, F.F., An Investigation Into the Use of Four-Bar Linkage Mechanism as Actuator for Hard-Disk Drive, IEEE Transactions on Magnetics, vol. 49, no. 6, Part: 1, 2013, 2466-2472

[3]   Hong Guo, Dayu Wang, and Jinquan Xu, Research on a High-Frequency Response Direct Drive Valve System Based on Voice Coil Motor, IEEE Transactions on Power Electronics, vol. 28, no. 5, 2013, 2483-2492

[4]   Shuai Wu, Zongxia Jiao, Liang Yan, Rui Zhang, Juntao Yu, Chin-Yin Chen, Development of a Direct-Drive Servo Valve With High-Frequency Voice Coil Motor and Advanced Digital Controller, IEEE/ASME Transactions on Mechatronics, vol. 19, no. 3, 2014, 932-942

[5]   Chien-Sheng Liu, Shun-Sheng Ko, and Psang-Dain Lin, Experimental Characterization of High-Performance Miniature Auto-Focusing VCM Actuator, IEEE Transactions on Magnetics, vol. 47, no. 4, 2011, 738-745

[6]   Pan, J.F., Yu Zou, Guangzhong Cao, Adaptive controller for the double-sided linear switched reluctance motor based on the nonlinear inductance modeling, IET Electric Power Applications, vol. 7, no. 1, 2013, 1-15

[7]   J.-K. Seok and S.-K. Kim, VCM controller design with enhanced disturbance decoupling for precise automated manufacturing processes, IET Electric Power Applications, vol. 6, no. 8, pp. 575-582

[8]   Yu Liu, Ming Zhang, Yu Zhu, Jin Yang and Badong Chen, Optimization of voice coil motor to enhance dynamic response based on an improved magnetic equivalent circuit model, IEEE Transactions on Magnetics, vol. 47, no. 9, 2011, 2247-2251

[9]   Chih-Min Lin, Hsin-Yi Li, A Novel Adaptive Wavelet Fuzzy Cerebellar Model Articulation Control System Design for Voice Coil Motors, IEEE Transactions on Industrial Electronics, vol. 59, no. 4, 2012, 2024-2033

[10] Chih-Min Lin Hsin-Yi Li, Adaptive Dynamic Sliding-Mode Fuzzy CMAC for Voice Coil Motor Using Asymmetric Gaussian Membership Function, IEEE Transactions on Industrial Electronics, vol. 61, no. 10, 2014

[11] Ching-LungTsai, Ti-ChungLee, Shir-Kuan Lin, Friction compensation of a mini voice coil motor by sliding mode control, IEEE International Symposium on Industrial electronics, 609-614, 2009.

[12] Tzuu-Hseng S. Li, Ching-Chang Chen, Yu-Te Su, Optical image stabilizing system using fuzzy sliding-mode controller for digital cameras, IEEE Transactions on Consumer Electronics, vol. 58, no. 2, 237-245, 2012

[13] Zhen Zhang, Peng Yan, Chao Lu, Tongtong Leng, Bofeng Liu, Time-varying internal model-based tracking control for a voice coil motor servo gantry, IEEE American Control Conference, 2872-2877, 2013

[14] Ion Boldea, Linear electric machines, drives, and MAGLEVs handbook, CRC Press, Boca Raton.

[15] Cristofaro Pompermaier, Kalluf Flavio Jorge Haddad, Alexandre Zambonetti, M. V. Ferreira da Luz, and Ion Boldea, Small Linear PM Oscillatory Motor: Magnetic Circuit Modeling Corrected by

Axisymmetric 2-D, IEEE transactions on industrial electronics, vol. 59, no. 3, 2012, 1389-1396

[16] Arun Gandhi and Leila Parsa, Thrust Optimization of a Flux-Switching Linear Synchronous Machine With Yokeless Translator, IEEE Transactions on Magnetics, vol. 49, no. 4, 2013, 1436-1443

[17] Lucian N. Tutelea, Myung Chin Kim, Marcel Topor, Ju Lee, and Ion Boldea, Linear Permanent Magnet Oscillatory Machine: Comprehensive Modeling for Transients With Validation by Experiments, IEEE transactions on industrial electronics, vol. 55, no. 2, 2008, 492-500

[18] S. C. Agarliţă, I. Boldea, F. Marignetti, and L.N. Tutelea, Position Sensorless Control of a Linear Interior Permanent Magnet Oscillatory Machine, with Experiments, 2010, 12th International Conference on Optimization of Electrical and Electronic Equipment, OPTIM 2010

[19] Cristian Lascu and Frede Blaabjerg, Super-twisting sliding mode direct torque control of induction machine drives, 2014 IEEE Energy Conversion Congress and Exposition (ECCE), 2014, 5116-5122.

[20] Lascu, Ion Boldea, and Frede Blaabjerg, Super-Twisting Sliding Mode Control of Torque and Flux in Permanent Magnet Synchronous Machine Drives, 39th IEEE Annual Conference Industrial Electronics Society, (IECON), 2013, 3171-3176

[21] Onofre A. Morfin, Riemann Ruiz-Cruz, Alexander G. Loukianov, Edgar N. Sánchez, M.I. Castellanos, and Fredy A. Valenzuela, Torque controller of a doubly-fed induction generator impelled by a DC motor for wind system applications, IET Renewable Power Generation, vol. 8, no. 5, 2014, 484-497

[22] Carlos E. Castaneda, Alexander G. Loukianov, Edgar N. Sanchez, and Bernardino Castillo-Toledo, Discrete-Time Neural Sliding-Mode Block Control for a DC Motor With Controlled Flux, IEEE Transactions on Industrial Electronics, vol. 59, no. 2, 2012, 1194-1207

[23] C. Evangelista, P. Puleston, F. Valenciaga, and L. M. Fridman, Lyapunov-Designed Super-Twisting Sliding Mode Control for Wind Energy Conversion Optimization, vol. 60, no. 2, 2013, 538-545

[24] Arie Levant and Miki Livne Uncertain disturbances' attenuation by homogeneous multi-input multi-output sliding mode control and its discretisation, IET Control Theory and Applications, vol. 9, no. 4 2015, 515-525

[25] F. F. M. El-Sousy, Robust wavelet-neural-network sliding-mode control system for permanent magnet synchronous motor drive, IET Electric Power Applications, vol. 5, no. 1, 2011, 113-132

[26] Chih-Min Lin ; Hsin-Yi Li, Adaptive Dynamic Sliding-Mode Fuzzy CMAC for Voice Coil Motor Using Asymmetric Gaussian Membership Function, IEEE Transactions on Industrial Electronics, vol. 61, no. 10, 2014, 5662-5671

[27] Lennart Ljung. System Identification—Theory for the User. Prentice-Hall

[28] Yuchao Shi, Kai Sun, Lipei Huang, Yongdong Li, Online Identification of Permanent Magnet Flux Based on Extended Kalman Filter for IPMSM Drive With Position Sensorless Control, IEEE Transactions on Industrial Electronics, vol. 59, no. 11, 2012, 4169-4178

[29] Pan, J.F., Yu Zou, Guangzhong Cao, Adaptive controller for the double-sided linear switched reluctance motor based on the nonlinear inductance modeling, IET Electric Power Applications, vol. 7, no. 1, 1-15

[30] J.F. Pan, Norbert C. Cheung, and Yu Zou, High-precision control of LSRM based X–Y table for industrial applications, ISA Transactions, vol. 52, 2013, 105-114

[31] K. David Young, Vadim I. Utkin, and Ü̈mit Ö̈zgü̈ner, A Control Engineer's Guide to Sliding Mode Control, IEEE Transactions on Control Systems Techonology, vol. 7, no. 3, 1999, 328-342

[32] Xiaoguang Zhang, Lizhi Sun, Ke Zhao, Li Sun, Nonlinear Speed Control for PMSM System Using Sliding-Mode Control and Disturbance Compensation Techniques, IEEE Transactions on Power Electronics, vol. 28, no. 3, 2013, Page(s): 1358 - 1365

[33] www.dspace.de

[34] Susperregui, A., Martinez, M.I., Zubia, I., Tapia, G., Design and tuning of fixed-switching-frequency second-order sliding-mode controller for doubly fed induction generator power control, IET Electric Power Applications, vol. 6, no. 9, 2012, 696-706